

LATTICE AND STRUCTURAL DISTORTIONS IN Gd³⁺ SUBSTITUTED LaMnO₃: INFRARED REFLECTIVITY MEASUREMENTS

J. AHMAD^{a,*}, G. ZAKIA^a, H. ABBAS^a, S. H. BUKHARI^b, U. NISSAR^a,
M. T. JAMIL^a, J. A. KHAN^a, U. AHMAD^a, S. A. ALI^a, T. SULTAN^c.

^aDepartment of Physics, Bahauddin Zakariya University, Multan 60800, Pakistan

^bDepartment of Physics, G. C. University Faisalabad, Layyah Campus, Layyah,
31200, Pakistan

^cDepartment of Civil Engineering, UCET, BZU Multan 60800, Pakistan

Polycrystalline La_{1-x}Gd_xMnO₃ multiferroics ($x = 0.0, 0.2, 0.4, 0.6, 0.8$ and 1.0) have been successfully synthesized by sol-gel combustion method. Rietveld refinement of X-ray diffraction (XRD) patterns clearly demonstrates a structural distortion from orthorhombic to rhombohedral perovskite-type structure, which suggests strong Jahn-Teller distortion. The infrared reflectivity (IR) spectra are measured at room temperature over a frequency range $30\text{-}7500\text{ cm}^{-1}$ by Fourier transform infrared (FTIR) spectrometer which exhibits several optical phonons. The resonant frequency ($\omega_{\text{TO}(j)}$), oscillator strength (S_j) and damping factor (γ_j) of various observed optical phonons have been determined by fitting the Lorentz oscillator model to the measured reflectivity spectra. The $\omega_{\text{TO}(j)}$ is found dependent on Gd concentration suggesting a strong electron-phonons interaction in the system. The optical conductivity $\sigma_1(\omega)$ calculated by using the Kramers-Kronig analysis of the IR spectra also confirms the phase transition on increasing the Gd concentration. The Born effective charges have been calculated using the transverse (TO) and longitudinal optical (LO) modes to understand the role of ionic polarization in the present multiferroic system.

(Received July 27, 2019; Accepted October 25, 2019)

Keywords: Sol Gel combustion synthesis, FTIR spectroscopy, Infrared reflectivity, Effective charges

1. Introduction

During the last few years $R_{1-x}A_x\text{MnO}_3$ manganites (R -- rare earth alkaline, A -- alkaline-metals) have attracted much interest because of their fascinating physical and optical properties to make such systems promising candidates for various technological applications such as magnetic sensors, magnetic switches and memory storage devices etc. [1]. Lanthanum manganite perovskites like LaMnO₃ exhibiting a special property of colossal magneto resistance (CMR) also have a potential application of catalytic and piezoelectric materials [2], and cathode materials for different solid state fuel cells [3-5]. Gadolinium is a logical choice as a dopant due to its materialization of magneto-caloric effects at room temperature and lowering of the Curie temperature on Gd substitution [6,7]. Along with the orthorhombic multiferroic manganites, GdMnO₃ possess a special position because its location on the magnetic phase diagram of RMnO_3 compounds is very close to the boundary of phase among A -type antiferromagnetic and cycloidal antiferromagnetic behaviours [8-10]. C.H. Booth *et al.* investigated that stoichiometrically LaMnO₃ have a distorted perovskite structure [11]. Furthermore, GdMnO₃ exhibits the phase transition from paramagnetic phase to the incommensurate antiferromagnetic phase [12].

Recently, enhanced multiferroic character has been observed in ABO₃ type polycrystals possessing nanosized particles as these exhibited distinctive electrical, magnetic, and optical properties far-off unusual from that of bulk counterparts, for the reason that of low standard

*Corresponding author: dr.j.ahmad@gmail.com

dimensions and quantum confinement effects [13]. Generally, multiferroics are classified into two main groups [14-16]. In type-I multiferroics, the ferroelectric order is occurred both above and below the Curie temperature, and large spontaneous polarization occurred. However, the occurrence of coupling between electric and magnetic order is weak. In type-II multiferroics, the large coupling between electric and magnetic sub-systems is observed and these show the giant magnetoelectric effects [17]. The changes in the mass effects, the bonding strength, and the bonding configuration in the host materials can be observed on substitutions at specific lattice sites that involve the vibrational characteristics. Thus, lattice vibrations of *A*- and *B*-site substitutions in the manganites investigated through Raman and infrared vibrational spectroscopy may help study the role of various atomic substitutions in the multiferrocity. Moreover, the infrared spectroscopy, in particular, is used for such systems to observe presence of strong electron-phonon interaction and also allow to study the possible softening of phonon modes driven ferroelectric transition or to extort the average value of Born effective charge throughout the LO and TO modes [12]. S.K. Park *et al.* [18] have reported charge ordered transition in $R_{1/3}\text{Sr}_{2/3}\text{FeO}_3$ which disappeared on replacing *R* site ion from *R* = La to smaller *R* ion of *R* = Gd because of weakening of the *p-d* hybridization which is otherwise strong in case of *R* = La. According to them, the compound possessing rhombohedral lattice distortion offered charge-ordered transition accompanied by charge disproportionation of Fe^{4+} into nominal Fe^{3+} and Fe^{5+} sites. Therefore, Gd substituted LaMnO_3 , being a sister compound of the $R\text{FeO}_3$ seems a good material to be investigated in order to study the effect of structural distortions on the associated physics of such systems.

In this paper, we report on the preparation of $\text{La}_{1-x}\text{Gd}_x\text{MnO}_3$ ($0.0 \leq x \leq 1.0$) using sol-gel combustion method. All the composition was identified by XRD pattern and an interesting phase transition confirmed by Rietveld analysis. The infrared reflectivity spectra have been analysed, the resonance frequency of the optical mode has been determined and utilized in calculation of the Born effective charges. The results have been discussed in order to understand the ionic polarization and associated multiferroicity in the $\text{La}_{1-x}\text{Gd}_x\text{MnO}_3$ system.

2. Experimental details

Polycrystalline $\text{La}_{1-x}\text{Gd}_x\text{MnO}_3$ ($x = 0.0, 0.2, 0.4, 0.6, 0.8, 1.0$) were synthesized using sol-gel combustion method. The starting materials $\text{La}(\text{NO}_3)_3 \cdot 6\text{H}_2\text{O}$, $\text{Gd}(\text{NO}_3)_3 \cdot 6\text{H}_2\text{O}$ and $\text{Mn}(\text{NO}_3)_2 \cdot 4\text{H}_2\text{O}$ in powder form were carefully weighed in their equivalent weight ratio stoichiometrically and dissolved in 50 ml distilled water. Citric acid was used as chelating agent with nitrate molar ratio of 1.5:1. The synthesis process starting from precursor to nanocrystalline powder involves three stages: precursor \rightarrow sol, sol \rightarrow gel and gel \rightarrow nanocrystalline powder reported elsewhere [19]. The pH value of the solutions was kept at approximately 7 ~ 8 using aqueous solution of ammonia. All the chemicals dissolved into the distilled water and stirred using hot plate magnetic stirrer in order to homogenise the solution. On heating the solution up to 70 °C, viscous gel was achieved which was further heated to 120 °C for 1 hour to obtain dried gel and grounded manually to make the fine powder.

The blackish dry fine powder was sintered at 900 °C for 8 hours in the box furnace (LHT 02/17) ground again manually to make pure form of powder, which was pressed into pellets using hydraulic press exerting pressure upto 30 KN. The phase of the samples was identified by the XRD operating with the standard $\text{Cu-K}\alpha$ radiation ($\lambda=1.5406\text{\AA}$). The Rietveld refinement was carried out to find out the structure by using the software JANA 2006. The reflectivity measurements were carried out at room temperature by using FTIR spectrometer (BRUKER VERTEX 80V) in the frequency range 30-7500 cm^{-1} covered using two beam splitter-detector combinations: KBr-DLaTGs and Mylar-DLaTGs.

3. Results and discussion

The structural investigation of $\text{La}_{1-x}\text{Gd}_x\text{MnO}_3$ was carried out by XRD pattern as shown in Fig. 1. The XRD data were analyzed by using the Rietveld refinement technique assuming the rhombohedral structure with the space group of $R\bar{3}c$ for base sample of LaMnO_3 .

GdMnO_3 is magnetoelectric at low temperature and belongs to the orthorhombic rare-earth manganite family. At the room temperature, this system predicts a distorted orthorhombic perovskite lattice structures with $Pnma$ or $Pbnm$ symmetry, as reported by Noda *et al.* and Pena *et al.* [20-21]. By increase in the concentration of Gd in LaMnO_3 for $x = 0.2, 0.4$ the pattern remains same and for $x = 0.6, 0.8$ and 1.0 , the structure were tartan with the orthorhombic structures different in space groups, which is the phase transition occurring at higher concentration from rhombohedral to orthorhombic. X. J. Hemberger *et al.* [10] also reported the orthorhombic structures of $\text{La}_{1-x}\text{Gd}_x\text{MnO}_3$ and phase transition from rhombohedral to orthorhombic were reported in $\text{Bi}_{1-x}\text{Ca}_x\text{Fe}_{1-x}\text{Mn}_x\text{O}_3$ systems [22]. F. Mizouri *et al.* also observed the same phase transition in the $\text{BiFeO}_{3-x}\text{Ba}_{0.9}\text{Ca}_{0.1}\text{Ti}_{0.9}\text{Sn}_{0.1}\text{O}_3$ ceramics as rhombohedral structure for $x=0.1$ and $x=0.2$ and orthorhombic for $x=0.4$ and $x=0.5$ [23]. The peaks profiles fitting were done by the pseudo-Voigt function. Some of the detectable impurity peaks were also observed in the higher concentration of Gd but no systematic increase in impurity observed. A close inspection of XRD spectra depicts the change in the behaviours of the peaks at the higher concentration of Gd. At the higher values of the Bragg's angles intensities of peaks reduced and the splitting of the peaks or doublets peaks for $x \geq 0.4$, this may be occurred due to different reasons like doping effects occupancy of multiplications both in Mn and La sites and detailed investigations of the phase occupancy also reported in the sodium based lanthanum magnanites by S. Roy *et al.* [24]. From Fig.1, the main peak at $\theta=34^\circ$ at $x=0.0$, which is the split peak becomes weak at the higher concentration of Gd indicates the structural distortion [25]. The behaviour of the lattice parameters a , b and c are tabulated in Table 1. and corresponding cell distortion and cell volume are shown in Fig. 2 and 3 respectively. By increasing the Gd concentration the lattice constants a and c slightly varied and a remarkable structural information can be deduced by the variation in the lattice constant b . These variations correspond to the rhombohedral to orthorhombic transition; which may be due to the difference in size of La and Gd atoms. The lattice parameters indicate that the system is getting distorted, which was also reported in case of $\text{LaMn}_{1-x}\text{Fe}_x\text{O}_3$ [26]. The change in the lattice parameters may be due to the deficiencies of oxygen atoms as also reported by A. Bhaskar in the study of $\text{Ca}_{1-x}\text{Gd}_x\text{MnO}_{3-\delta}$ [27].

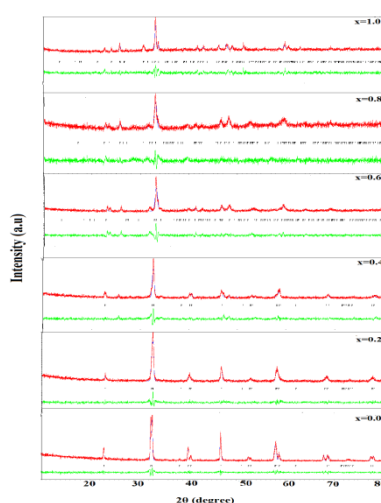


Fig. 1. Typical X-ray diffraction profiles for $\text{La}_{1-x}\text{Gd}_x\text{MnO}_3$ ($x=0.0, 0.2, 0.4, 0.6, 0.8, 1.0$). Key: observed data (red) and calculated profile (blue), difference plots (green) drawn below each profile, and tick marks (black) represent allowed Bragg reflections.

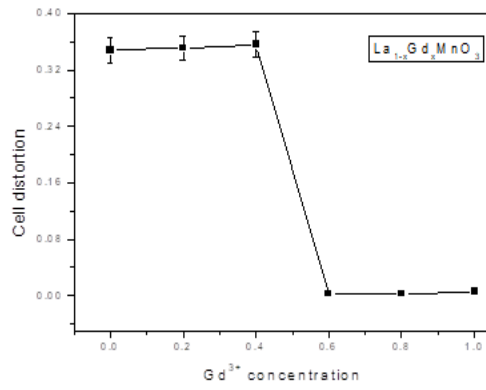


Fig. 2. Cell distortion as a function of Gd concentration for $La_{1-x}Gd_xMnO_3$ ($x=0.0, 0.2, 0.4, 0.6, 0.8, 1.0$).

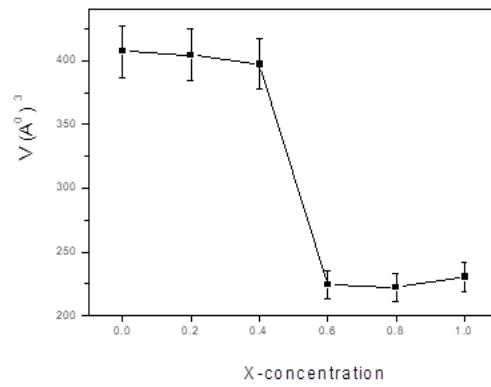


Fig. 3. Cell volume as a function of Gd concentration for $La_{1-x}Gd_xMnO_3$ ($x=0.0, 0.2, 0.4, 0.6, 0.8, 1.0$).

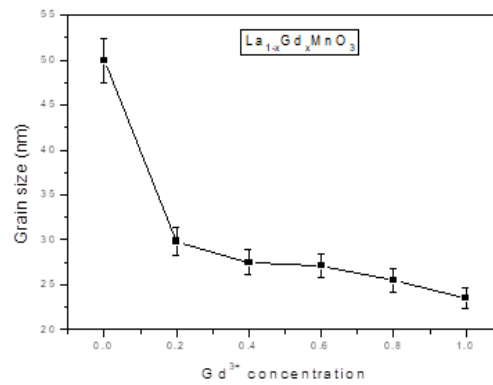


Fig. 4. Variation of grain size with Gd concentration for $La_{1-x}Gd_xMnO_3$ ($x=0.0, 0.2, 0.4, 0.6, 0.8, 1.0$).

Table 1. The lattice parameters and the unit-cell volume for different compositions of $\text{La}_{1-x}\text{Gd}_x\text{MnO}_3$ ($x=0.0, 0.2, 0.4, 0.6, 0.8, 1.0$) samples obtained from Rietveld refinement.

$\text{La}_{1-x}\text{Gd}_x\text{MnO}_3$ ($0 \leq x \leq 1.0$)	a (Å)	b (Å)	c (Å)	Unit cell volume (Å ³)	Structure symmetry
$X=0.0$	5.53	5.53	13.32	407.34	Rhombohedral
$X=0.2$	5.51	5.51	13.31	404.34	Rhombohedral
$X=0.4$	5.47	5.47	13.28	397.34	Rhombohedral
$X=0.6$	5.45	5.55	7.41	224.13	Orthorhombic
$X=0.8$	5.33	5.62	7.42	222.26	Orthorhombic
$X=1.0$	5.31	5.84	7.43	230.41	Orthorhombic

The particle size or grain size is shown in Fig. 4, which has been calculated from XRD samples by using the general Debye Scherrer formula [28]

$$D = k \lambda / \beta \cos \Theta \quad (1)$$

where, $k = 0.9$, $\lambda = 1.5406 \text{ \AA}$ is the wavelength of Cu-K α radiation, β is the full width of half maximum of diffraction peak and θ is the Bragg's angle.

The grain size of the undoped LaMnO_3 '50 nm' gradually decreased by increasing the concentration of Gd atoms. It is thought that the lowering of calcination temperature causes smaller size nanoparticles, on the other hand higher calcination temperature commonly causes the larger particle size and also wider particle size distribution [29].

To investigate response of atoms and group of atoms to the electromagnetic radiation for $\text{La}_{1-x}\text{Gd}_x\text{MnO}_3$; $x = 0.0, 0.2, 0.4, 0.6, 0.8$ and 1.0 , the infrared reflectivity spectra measured using FTIR spectroscopy are shown in Fig. 5 and 6. The reflectivity spectrum of undoped LaMnO_3 was measured from 0 - 5000 cm^{-1} and the main phonon bands along with some overtones were observed, as shown in Fig. 5. Above 800 cm^{-1} the spectrum is almost flat and structure-less, signal to noise ratio is high below $\sim 100 \text{ cm}^{-1}$ and phonons could not be resolved. Therefore, we focused on spectra from 100 to 800 cm^{-1} for further analysis.

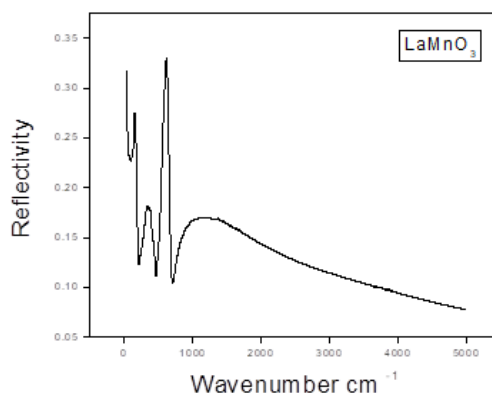


Fig. 5. Reflectivity spectrum for LaMnO_3 .

The analysis of infrared reflectivity spectra has been carried out by fitting Lorentz oscillator model [30,31]:

$$\epsilon(\omega) = \epsilon_{\infty} + \frac{\sum_j \omega_{TO(j)}^2 T O(j) S_j}{\omega_{TO(j)}^2 - \omega^2 - i\omega\gamma_j} \quad (2)$$

where, ϵ_{∞} is the high frequency dielectric constant, $\omega_{TO(j)}$ is the resonant frequency of transverse optical (TO) j th phonon mode, γ_j is the damping factor and S_j is the oscillator strength of j^{th}

optical phonon modes. To achieve the reflectivity at near normal incidence, we use the Fresnel formula to correlate the dielectric function with the IR reflectivity, given as [32]:

$$R(\omega) = \left| \frac{\sqrt{\epsilon(\omega)} - 1}{\sqrt{\epsilon(\omega)} + 1} \right|^2 \quad (3)$$

There are four main optical phonons occur in the base sample (Fig. 6) and two new phonons observed by increasing the Gd concentration $x=0.6, 0.8$, which are associated to the phase transition. The phase transition also becomes clear with increasing the concentration of Gd at $x=1.0$ having spectra more rich in the phonons whose IR data is published in our earlier work [12]. IR phonon spectrum can be classified into three optical phonon bands that correspond to the normal modes of the ideal cubic $RMnO_3$ perovskite, low frequency external phonon band ($\omega < 290 \text{ cm}^{-1}$), Bending phonon band at intermediate range ($290 \text{ cm}^{-1} < \omega < 590 \text{ cm}^{-1}$) and high frequency stretching band ($\omega > 590 \text{ cm}^{-1}$) [33]. The TO modes of 162, 166, 176, 179 and 180 cm^{-1} contribute the motion of Gd atoms relative to MnO_6 octahedral [12]. As Gd atom is heavier so it vibrates at low frequency. The phonons of 255, 333, 336, 384 and 406 cm^{-1} cause the complex motion of Mn atoms relative to the oxygen atoms. Moreover, the phonons of 584, 588, 594, 603 and 614 cm^{-1} predict the asymmetric stretching which indicates the phase distortion [34].

Interestingly, a smooth broadening of most of the modes was identified. It can be ascribed to the disorder which may be introduced by the substitution of Gd atoms for La atoms, which is analogous to what observed for $YMn_{1-x}Fe_xO_3$ ($0 \leq x \leq 0.20$) [35]. N.E. Massa *et.al.* associated hardening (softening) of phonons with shorter (longer) bond length [36]. In our data the doping of Gd in $LaMnO_3$, results in softening initially for first three TO modes indicating longer bond length between the La atoms and Gd, which shifts toward the hardening in the fourth TO mode showing the decrease in the bond length. From ambient $x=0.2, 0.4, 0.6$ and 0.8 no significant change in the spectra is observed other than change in damping parameter of the TO and LO optical modes as is also reported in the temperature dependent infrared study of $Ti_{1.5}Bi_{0.5}Mn_2O_7$ [36], but for the further increase in the concentration of Gd atoms more phonons appear due to change in the phase. Interestingly, the hardening of phonons for $x=0.8$ corresponds the change in structural distortion as reported in case of $BiFeO_3$ single crystal [30]. TO phonon frequency (ω_{TO}) obtained from the peak position of reflectivity spectra as a function of Gd^{3+} concentration.

Table 2. Lorentz Oscillators best fit parameters extracted from fitting to the infrared reflectivity spectra measured at room temperature for the $La_{1-x}Gd_xMnO_3$.

x	0	0.2	0.4	0.6	0.8
$\omega_{TO1} (\text{cm}^{-1})$	588	584	614	594	603
$\omega_{TO2} (\text{cm}^{-1})$	384	383	406	382	381
$\omega_{TO3} (\text{cm}^{-1})$	336	333	327	331	331
$\omega_{TO3'} (\text{cm}^{-1})$	-----	-----	-----	255	254
$\omega_{TO4} (\text{cm}^{-1})$	162	166	176	180	179
s_1	0.908	0.7	0.507	0.575	0.555
s_2	0.339	0.013	0.323	0.005	0.006
s_3	0.402	0.725	0.528	0.536	0.942
$s_{3'}$	-----	-----	-----	0.257	0.606
s_4	1.91	1.627	1.497	1.127	2.385
$\gamma_1 (\text{cm}^{-1})$	79.275	88.513	101.825	108.524	98.606
$\gamma_2 (\text{cm}^{-1})$	71.023	13.389	78.951	7.504	6.778
$\gamma_3 (\text{cm}^{-1})$	81.849	130.183	122.593	126.502	127.712
$\gamma_{3'} (\text{cm}^{-1})$	-----	-----	-----	59.538	65.062
$\gamma_4 (\text{cm}^{-1})$	57.823	59.672	50.983	50.371	59.925
ϵ_∞	2.449	2.329	3.12	2.294	3.18
ϵ_0	6.008	5.394	5.975	4.794	7.674

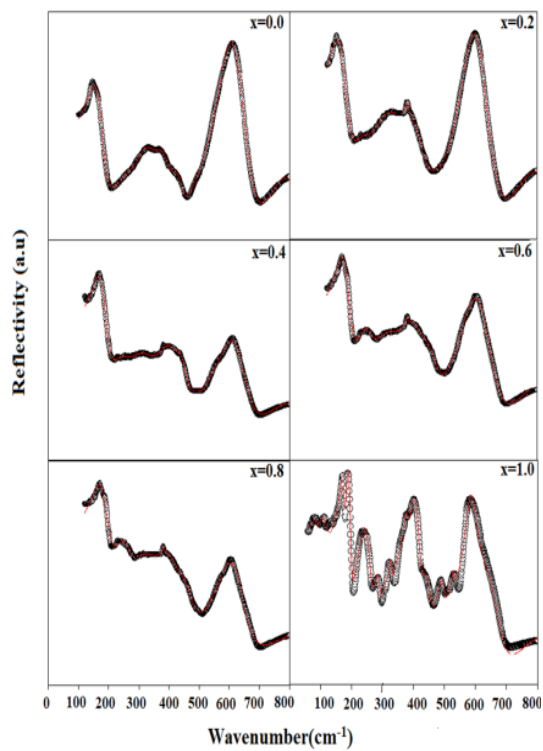


Fig. 6. IR reflectivity spectra for $La_{1-x}Gd_xMnO_3$.

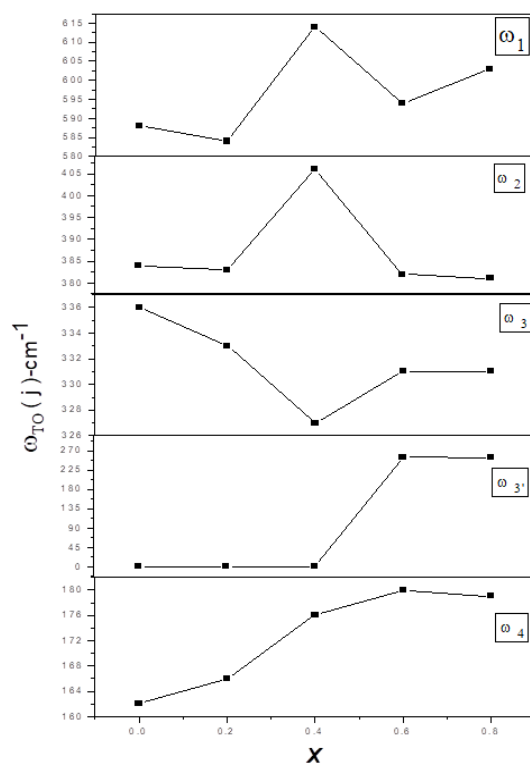


Fig. 7. Compositional Dependence of Transverse optical frequency.

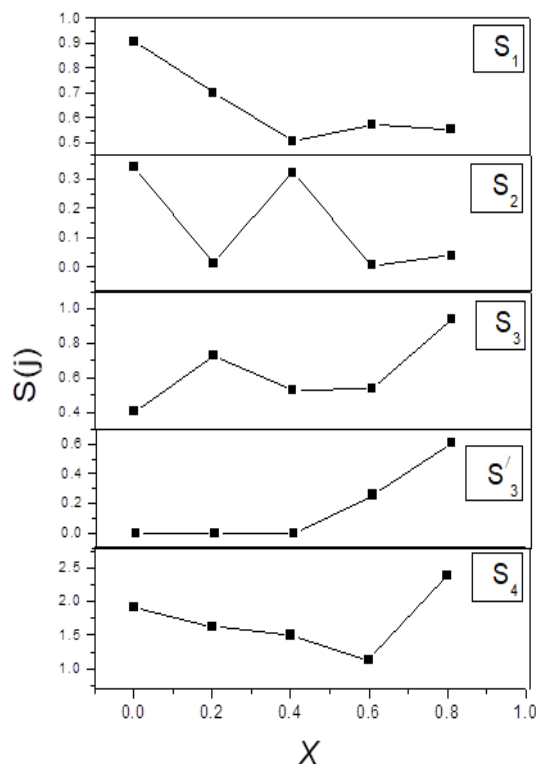


Fig. 8. Oscillator strength as a function of x for $\text{La}_{1-x}\text{Gd}_x\text{MnO}_3$.

Fig. 7 shows that the optical frequency of the fourth TO mode get hardens on Gd^{3+} doping. This may be because of the coupling of these phonons with electronic degree of freedom resulting in phonon-electron interaction in the material. The oscillator strength as a function of Gd doping for observed phonons is plotted in Fig. 8. The vibrational frequencies values have a tendency to underestimate and overestimate the splitting of TO-LO for the oscillator strengths [37].

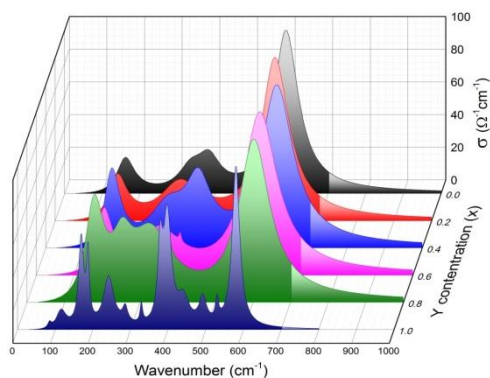


Fig. 9. The real part of optical conductivity ($\sigma_1(\omega)$) extracted from the infrared reflectivity pattern.

The optical conductivity of $\text{La}_{1-x}\text{Gd}_x\text{MnO}_3$ (for $x = 0, 0.2, 0.4, 0.6$ and 0.8) has been calculated from measured IR spectra. We calculate the $\sigma_1(\omega)$ spectra for the electronic structure of $\text{La}_{1-x}\text{Gd}_x\text{MnO}_3$ investigated quantitatively, by using relation [32],

$$\sigma_1(\omega) = \omega \epsilon_2 / 4\pi \quad (4)$$

where, $\sigma_1(0)$ is zero having presence that there is no contribution from free carriers at low frequency range and also suggest the localized charge carrier. From Fig. 9, it can be seen that the number of phonons increased by increasing the concentration of Gd. Interestingly, the peaks below 200 cm^{-1} splits into two main peaks which correspond to the phase transition and two new small peaks appeared between 400 and 600 cm^{-1} which is indication of strong distortion in MnO_6 octahedra that was also observed in doping of Ce in LaMnO_3 by J. Ahmad *et al.* [38].

It is also interesting to discuss the behaviour of high frequency dielectric constant and static dielectric constant with increasing Gd doping. The static dielectric constant is due to phonon and electron contributions. The high-frequency dielectric constant is by electronic absorption process which was obtained from the room-temperature frequency-independent reflectivity tails above of the phonon frequencies. It can be noticed that high frequency dielectric constant increases with adding Gd^{3+} , as shown in Fig. 10.

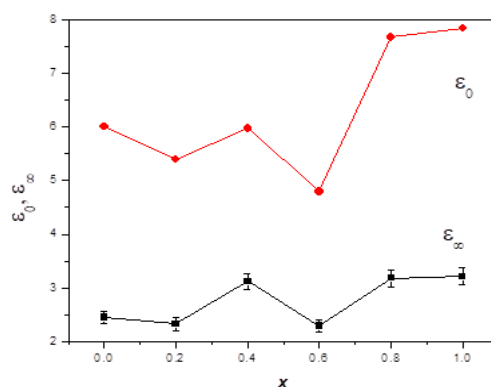


Fig. 10. The changes of high frequency ϵ_∞ and static dielectric constant $\epsilon_{(0)}$ of $\text{La}_{1-x}\text{Gd}_x\text{MnO}_3$ for compositions $x = 0.0, 0.2, 0.4, 0.6, 0.8$ and 1.0 .

R.J. Gonzalez *et al.* describe for refractive index $\epsilon=n^2$, where n is refractive index, our ϵ_0 values describe the refractive indices of 2.41 and 2.33. On the other hand reported values of n in the visible region are 2.49 and 2.56, which can affect the shape of reflectivity spectrum and TO modes also closer to our reported values [37].

4. Born effective charge

The Born effective charge demonstrates the change of polarization that would be observed under the condition of zero macroscopic electric field. It involves both static and dynamic contributions towards the electric dipole moment. For simple materials with purely ionic character like that binary crystals and simple semiconductors, the Born effective charge value corresponds to the nominal ionic charges. It could deviate remarkably in the ferroelectrics and it succeeds to predict accurately the spontaneous polarization. The Born effective charges can be calculated from LO-TO phonon frequency splitting using the relation [39]:

$$\frac{4\pi}{v_c} \sum_{k=1}^n \frac{z_k^*{}^2}{m_k} = 4\pi^2 \sum_{j=1}^N (\omega_{LOj}^2 - \omega_{TOj}^2) \quad (5)$$

where, v_c represents the unit cell volume, j represents j^{th} phonon mode, and m_k mass of k^{th} atom and k is the sum over all atoms with mass m_k . Interestingly, that Born effective charges comprise together ionic, static and dynamics electronic assistances to the dipole moment optimistic through the electric field. In any oxide crystal system, the evaluation of the Born effective charges can be written on basis of transverse optical (TO) mode and longitudinal optical (LO) mode through the phonons frequency [40]. Born effective charges (\vec{Z}_k) are also clue of dealings pro Coulomb long

range force as compared to the short range force, which also leads to the transitions in ferroelectrics [41]. Born effective charges calculated for phonon modes for all Gd concentrations are given below in Fig. 11.

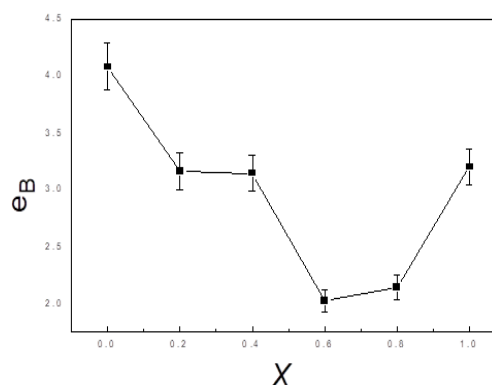


Fig. 11. Born effective charges of $\text{La}_{1-x}\text{Gd}_x\text{MnO}_3$ as a function of Gd composition.

From the figure, it can be seen clearly that the Born effective charge decreases with increasing Gd concentration. There is a slight decreased behaviour observed in Born effective charge for $x=0.8$ and for $x=1.0$ the value increased which provide the sustain in the ferroelectric polarization phenomenon reported in our earlier work [12].

5. Conclusions

$\text{La}_{1-x}\text{Gd}_x\text{MnO}_3$ multiferroics were synthesized by sol-gel method for the composition of $x=0.0, 0.2, 0.4, 0.6, 0.8$ and 1.0 . The structural distortion was revealed from the XRD pattern, the Rietveld refinement of the XRD pattern revealed the phase transition from rhombohedral to the orthorhombic, which may be responsible for ferroelectric character in these materials. The observed deviations in structure from the ideal perovskite cubic phases may be attributed to the tilting of MnO_6 octahedra, which clearly manifested itself as IR phonons.

Furthermore, Gd^{3+} substitution in LaMnO_3 resulted in increased number of phonons and enhanced phonon mode splitting suggesting significant lattice distortion. The variation in Born effective charges are indicative of shift of ionicity due to electric and magnetic polarization on the Gd^{3+} substitution in LaMnO_3 multiferroics.

References

- [1] G. De Marzi, Z. V. Popovic, A. Cantarero, Z. D. Mitrovic, N. Paunovic, J. Bok, F. Sapina, *Phys. Rev. B* **68**, 064302 (2003).
- [2] N. Rezlescu, E. Rezlescu, C. Doroftei, P. D. Popa, M. Ignat, J. Diges. *Nanomater. & Biostruc.* **8** (2013).
- [3] M. Gajek, M. Bibes, S. Fusil, K. Bouzehouane, J. Fontcuberta, A. Barthelemy, A. Fert, *Natu. Mater.* **6**, 296 (2007).
- [4] W. Prellier, E. R. Buzin, C. Simon, B. Mercey, M. Hervieu, S. D. Brion, G. Chouteau, *Phys. Rev. B* **66**, 024432 (2002).
- [5] S. Chattopadhyay, T. K. Nath, *Curr. Appl. Phys.* **11**, 1153 (2011).
- [6] H. Chen, C. Lin, D. Dai, *J. Magn. Magn. Mater.* **257**, 254 (2003).
- [7] A. Krichene, W. Boujelben, A. Cheikhrouhou, *J. Allo. Comp.* **550**, 75 (2013).
- [8] T. Kimura, T. Kimura, S. Ishihara, H. Shintani, T. Arim, K. Takahashi, K. Ishizaka, Y. Tokura, *Phys. Rev. B* **68**, 060403 (2003).
- [9] T. Kimura, G. Lawes, T. Goto, Y. Tokura, A. P. Ramirez, *Phys. Rev. B* **71**, 224425 (2005).

- [10] J. Hemberger, S. Lobina, H. A. K. V. Nidda, N. Tristan, V. Y. Ivanov, A. A. Mukhin, A. M. Balbashov, A. Loidl, *Phys. Rev. B* **70**, 024414 (2004).
- [11] C. H. Booth, F. Bridges, G. H. Kwei, J. M. Lawrence, A. L. Cornelius, J. J. Neumeier, *Phys. Rev. B* **57**, 10440 (1998).
- [12] S. H. Bukhari, J. Ahmad, *Act. Phys. Polo. A* **129**, 43-48 (2016).
- [13] Y. Wang, G. Xu, Z. Ren, X. Wei, W. Weng, P. Du, G. Shen, G. Han, *J. Amer. Cera. Soci.* **90**, 2615-2617 (2007).
- [14] D.I. Khomskii, *J. Magn. Magn. Mater.* **306**, 1-8 (2006).
- [15] D. Khomskii, *Phys.* **2**, 20 (2009).
- [16] T. Lottermoser, D. Meier, R.V. Pisarev, M. Fiebig, *Phys. Rev. B*, **80**, 100101 (2009).
- [17] C. Kadlec, V. Goian, K. Z. Rushchanskii, P. Kuzel, M. Lezaic, K. Kohn, R. V. Pisarev, S. Kamba, *Phys. Rev. B*, **84**, 174120 (2011).
- [18] S. K. Park, T. Ishikawa, Y. Tokura, J. Q. Li, Y. Matsui, *Phys. Rev. B*, **60**, 10788 (1999).
- [19] G. Xiong, Z. L. Zhi, X. Yang, L. Lu, X. Wang, *J. Mater. Scie. Lett.* **16**, 1064 (1997).
- [20] K. Noda, S. Nakamura, J. Nagayama, H. Kuwahara, *J. Appl. Phys.* **97**, 10C103 (2005).
- [21] O. Pena, M. Bahout, K. Ghanimi, P. Duran, D. Gutierrez, C. Moure, *J. Mater. Chem.* **12**, 2480-2485 (2002).
- [22] R. Palai, R. S. Katiyar, H. Schmid, P. Tissot, S. J. Clark, J. Robertson, S. A. T. Redfern, G. Catalan, J. F. Scott, *Phys. Rev. B*, **77**, 014110 (2008).
- [23] F. Mizouri, I. Kallel, N. Abdelmoula, D. Mezzane, H. Khemakhem, *J. Alloy. Comp.* **731**, 458-464 (2018).
- [24] S. Roy, Y. Q. Guo, S. Venkatesh, N. Ali, *J. Phys. Condens. Matt.* **13**, 9547 (2001).
- [25] M. Muneeswaran, J. W. Jang, B. C. Choi, J. H. Jeong, N. V. Giridharan, *Structural, J. Mater. Scien. Mater. Electr.* **28**, 16788-16796 (2017).
- [26] W. Khan, A. H. Naqvi, M. Gupta, S. Husain, R. Kumar, *J. Chem. Phys.* **135**, 054501 (2011).
- [27] A. Bhaskar, C.-J. Liu, J. J. Yuan, *Scienti. Wor. Jour.* **2012** (2012).
- [28] A. L. Patterson, *Phys. Rev.* **56**, 978 (1939).
- [29] A. Ahmad, H. Bae, I. Rhee, *AIP Advan.* **8**, 015108 (2018).
- [30] R. Lobo, R. L. Moreira, D. Lebeugle, D. Colson, *Phys. Rev. B* **76**, 172105 (2007).
- [31] M. Zaghrioui, V. T. Phuoc, R. A. Souza, M. Gervais, *Phys. Rev. B* **78**, 184305 (2008).
- [32] J. Ahmad, S. H. Bukhari, M. T. Jamil, M. K. Rehmani, H. Ahmad, T. Sultan, *Advan. Condens. Matt. Phys.* 2017 (2017).
- [33] J. Kim, S. Jung, M. S. Park, S.-I. Lee, H. D. Drew, H. Cheong, K. H. Kim, E. J. Choi, *Phys. Rev. B* **74**, 052406 (2006).
- [34] K. Sigrist, *Thermochi. Act.* **311**, 213 (1998).
- [35] M. Zaghrioui, V. T. Phuoc, *Sol. Sta. Comm.* **151**, 1704 (2011).
- [36] N. E. Massa, J. A. Alonso, M. J. M. Lope, M. T. Casais, H. Salva, *Phys. Rev. B* **60**, 7445 (1999).
- [37] R. J. Gonzalez, R. Zallen, H. Berger, *Phys. Rev. B* **55**, 7014 (1997).
- [38] J. Ahmad, U. Ahmad, S. H. Bukhari, *Chin. Jour. Phys.* DOI (2018).
- [39] J. Ahmad, H. Abbas, S. H. Bukhari, M. Tufiq Jamil, U. Nissar, J. A. Khan, S. A. Ali, *J. Ovon. Research.* **14**(4), 429 (2018).
- [40] F. Gervais, *Sol. Sta. Commu.* **18**, 191-198 (1976).
- [41] P. Ghosez, X. Gonze, P. Lambin, J. P. Michenaud, *Phys. Rev. B* **51**, 6765 (1995).